Published in final edited form as:
Nanoscale. 2021 January 08; 13(1): 163–174. doi:10.1039/d0nr05489e.

Silver telluride nanoparticles as biocompatible and enhanced contrast agents for X-ray imaging: an *in vivo* breast cancer screening study†

Lenitza M. Nieves[a], **Jessica C. Hsu**[b], **Kristen C. Lau**[b], **Andrew D. A. Maidment**[c], **David P. Cormode**[a,b,c]

[a]Biochemistry and Molecular Biophysics Department, University of Pennsylvania, Philadelphia, USA

[b]Bioengineering Department, University of Pennsylvania, Philadelphia, USA

[c]Radiology Department, University of Pennsylvania, Philadelphia, USA

Abstract

Silver sulfide nanoparticles (Ag_2S NPs) have gained considerable interest in the biomedical field due to their photothermal ablation enhancement, near-infrared fluorescence properties, low toxicity levels, and multi-imaging capabilities. Silver telluride nanoparticles (Ag_2Te NPs) have similar properties to Ag_2S NPs, should also be stable due to an extremely low solubility product and should generate greater X-ray contrast since tellurium is significantly more attenuating than sulfur at diagnostic X-ray energies. Despite these attractive properties, Ag_2Te NPs have only been studied *in vivo* once and at a low dose (2 mg Ag per kg). Herein, for the first time, Ag_2Te NPs' properties and their application in the biomedical field were studied *in vivo* in the setting requiring the highest nanoparticle doses of all biomedical applications, *i.e.* X-ray imaging. Ag_2Te NPs were shown to be stable, biocompatible (no acute toxicity observed in the cell lines studied or *in vivo*), and generated higher contrast, compared to controls, in the two X-ray imaging techniques studied: computed tomography (CT) and dual-energy mammography (DEM). In summary, this is the first study where Ag_2Te NPs were explored *in vivo* at a high dose. Our findings suggest that Ag_2Te NPs provide strong X-ray contrast while exhibiting excellent biocompatibility. These results highlight the potential use of Ag_2Te NPs in the biomedical field and as X-ray contrast agents for breast cancer screening.

---

†Electronic supplementary information (ESI) available: Synthesis and characterization of Ag NPs and Ag_2S (TEM micrographs, EDX spectra, UV-visible absorption spectra, XPS spectra, and XRD patterns), FT-IR spectra of the different nanoparticles formulations, 11-mercaptoundecanoic acid coated Ag_2Te as z-potential and stability controls, Ag^+ ion release from Ag_2Te NPs, photograph of DEM phantom, DEM energy pair optimization data, and the quantification of the change in CT attenuation in organs of mice injected with Ag_2S NPs. See DOI: 10.1039/d0nr05489e

david.cormode@pennmedicine.upenn.edu; Tel: +1 215-662-7868, +1 215-615-4656.

Author contributions The project was designed by L. M. N., A. D. A. M, and D. P. C. L. M. N., J. C. H., K. C. L., and D. P. C. performed the experiments. L. M. N and D. P. C. wrote the manuscript. All authors contributed to and have approved the final version of the manuscript.

Conflicts of interest D. P. C. and A. D. A. M. are named as inventors on patent applications concerning silver-based contrast agents. They also hold stock in Daimroc Imaging, a company that is seeking to commercialize such agents.

Nanomaterials are known for their unique physical and chemical properties including their exceptional optical characteristics, ability to be engineered to obtain desired properties through the modification of their surface, size, and composition, as well as their tunable pharmacokinetics. These unique characteristics have led to the exploration of nanomaterials in biomedical applications,[1] such as fluorescence imaging and sensing probes,[2] drug delivery vehicles,[3] theranostic agents,[4] and contrast agents for several medical imaging techniques,[5–8] and have been key to innovation and progression in the field. Recently, several groups, including ours, have studied silver chalcogenides such as silver sulfide (Ag_2S NP) and silver selenide nanoparticles (Ag_2Se NP) in the biomedical field due to their photothermal ablation enhancement, near-infrared fluorescence properties, low toxicity levels, and X-ray contrast generation.[9–14]

In addition to Ag_2S and Ag_2Se, the silver chalcogenide group also includes silver telluride (Ag_2Te). Ag_2Te has an extremely low solubility product ($K_{sp} = 2 \times 10^{-72}$),[15] much lower than those of Ag_2S and Ag_2Se (6×10^{-50} and 3×10^{-65}, respectively), and could consequently also have excellent stability and biocompatibility.[16,17] Moreover, tellurium generates similar X-ray attenuation to silver, whereas the attenuation of sulfur and selenium is negligible at diagnostic energies, therefore the X-ray attenuation of Ag_2Te should be substantially higher than for Ag_2S and Ag_2Se.[18] However, despite their outstanding properties, Ag_2Te NPs have been rarely explored in biomedical applications. Ag_2Te NPs have been explored as surface-enhanced Raman sensors and their NIR-II imaging properties have been characterized.[19,20] However, only one other study to date has explored the biomedical application of Ag_2Te NPs *in vivo*, and at a low Ag_2Te NP dose.[21]

In this study, we propose taking advantage of the attractive properties of Ag_2Te NP to further explore their application in the biomedical field. We, therefore, tested Ag_2Te NPs in the setting that requires the highest nanoparticle doses of all biomedical applications, *i.e.* X-ray imaging.[22] We hypothesized that Ag_2Te NPs can be excellent contrast agents for two main X-ray imaging modalities: computed tomography (CT) and dual-energy mammography (DEM). CT is the most widely used X-ray imaging technique for whole-body imaging, while DEM is a newly developed multi-energy mammography technology approved for breast cancer screening. Currently, both X-ray imaging modalities rely on iodine-based contrast agents, which have been linked with contrast-induced nephropathy and allergic reactions.[23] We hypothesize that Ag_2Te NPs will meet the needs of both X-ray imaging techniques, with higher contrast than Ag_2S NPs due to the presence of tellurium, while exhibiting excellent biocompatibility. In addition to silver chalcogenides, other metal nanoparticles including gold (Au) and Bismuth (Bi) have been widely used in X-ray imaging owning their high *k*-edge and X-ray attenuation coefficient in addition to their good biocompatibility.[5,24] However, the *k*-edges of these materials are not suitable DEM X-ray imaging for breast cancer screening, where Ag_2Te exhibits high contrast.[18] In addition, silver chalcogenides are of significantly lower cost than Au nanoparticles (*i.e.* \$63 per g Au *vs.* \$0.89 per g Ag), and thus could be more accessible to patients.

In this study, Ag_2Te NPs were characterized using transmission electron microscopy (TEM), dynamic light scattering (DLS), UV-vis spectroscopy, energy dispersive X-ray spectroscopy (EDX), X-ray powder diffraction (XRD) as well as inductively coupled plasma optical emission spectroscopy (ICP-OES). We tested the biocompatibility of the nanoparticles through a series of experiments both, *in vitro*, through cell viability in different cell lines, and *in vivo*, through histology analysis. Moreover, their ability to be used as X-ray contrast agents was explored in an *in vitro* setting using different X-ray imaging modality phantoms, as well as *in vivo* through CT imaging of breast cancer tumor-bearing mice. Furthermore, the biodistribution of these nanoparticles in mice was also analyzed.

Materials and methods

Materials

Silver nitrate ($AgNO_3$), sodium borohydride ($NaBH_4$), and sodium citrate ($Na_3C_6H_5O_7$) were purchased from Sigma-Aldrich (St Louis, MO). Sodium tellurite (Na_2TeO_3) was purchased from Alfa Aesar (Haverhill, MA). Hydrazine (N_2H_4) 80% and nitric acid (HNO_3) were purchased from Acros Organics (Thermo Fisher Scientific, NJ) and Fisher Chemical (Thermo Fisher, Waltham, MA), respectively. Monofunctional PEG thiol (mPEG-SH) 5 K was purchased from Creative PEGworks (Chapel Hill, NC). Milli-Q deionized water (18.2 MΩ cm) was used throughout the experiments.

Nanoparticle synthesis

Silver telluride nanoparticles.—The synthesis protocol of silver telluride nanoparticles (Ag_2Te NPs) was adapted from a previous report.[20] In brief, a 9 mL aqueous solution containing 5 mM of sodium tellurite, 10 mM of silver nitrate, and 30 mM of mPEG-SH 5 K was prepared. 1 mL of hydrazine was quickly added to the previous solution. The mixture was then heated to 90 °C for 30 minutes under constant magnetic stirring. After the reaction was completed, the product was washed thrice, with DI water, by centrifugation using 10 kDa ultrafiltration molecular weight cut-off tubes (MWCO) at 4000 rpm. Following the third wash, the nanoparticles were dispersed in DPBS and then washed by centrifugation at the above-mentioned speed and using the same size MWCO tubes. The nanoparticles were then concentrated to a final volume of 1 mL and filtered through a 0.22 μm filter. The filtered nanoparticles were then stored at 4 °C for further use.

Silver nanoparticles.—Silver nanoparticles (Ag NPs) were prepared as described in our previous work.[25] In brief, 1.25 mL of 0.1 M sodium citrate were added to 500 mL of DI water, followed by the addition of 1.25 mL of 0.1 M silver nitrate and 5 mL of 0.1 M sodium borohydride. Next, 5 mL of 12.5 mg mL^{-1} mPEG-SH-5 K were added to the reaction, which was left to stir overnight. The resulting particles were purified thrice with DI water and concentrated by centrifugation using 10 kDa MWCO tubes at 4000 rpm. Following the third wash, the nanoparticles were dispersed in DPBS and then washed by centrifugation at the above-mentioned speed and using the same size MWCO tubes. The nanoparticles were then concentrated to a final volume of 1 mL and filtered through a 0.22 μm filter. The filtered nanoparticles were then stored at 4 °C for further use.

Silver sulfide nanoparticles.—Silver sulfide nanoparticles (Ag_2S NPs) were prepared by mixing 0.375 mmol of $AgNO_3$ and 0.012 mmol of mPEG-SH 5 K in 75 mL of DI water, followed by the rapid addition of 0.38 mmol of Na_2S in 25 mL of DI water at ambient conditions. The reaction was allowed to stir overnight at room temperature. The resulting particles were purified three times with DI water and concentrated by centrifugation using 10 kDa MWCO tubes at 4000 rpm. Following the third wash, the nanoparticles were dispersed in DPBS and then washed by centrifugation at the above-mentioned speed and using the same size MWCO tubes. The nanoparticles were then concentrated to a final volume of 1 mL and filtered through a 0.22 μm filter. The filtered nanoparticles were then stored at 4 °C for further use.

Nanoparticle characterization

Dynamic light scattering and zeta potential.—The hydrodynamic diameter and zeta potential of the nanoparticles were measured using a Zetasizer (Nano-ZS 90, Malvern instrument, Malvern, UK). The number mean was reported for the hydrodynamic diameter. All measurements were performed at 25 °C.

Transmission electron microscopy.—Nanoparticle core size was measured as described previously.[9,26] JEOL 1010 and Tecnai T12 electron microscopes were used with an acceleration voltage of 80 and 100 kV, respectively. 10 μL of the sample were placed onto Formvar carbon-coated copper grids with 200 mesh (Electron Microscopy Sciences, Hatfield, PA) and allowed to dry before imaging. ImageJ (National Institutes of Health, Bethesda, MD) was used to measure the core diameter of individual nanoparticles.

UV/visible absorption spectroscopy.—UV/visible spectra of silver telluride nanoparticle were recorded using a Genesys 150 UV/visible spectrophotometer (Thermo Scientific, USA). In brief, 5 μl of the nanoparticle stock were diluted with 995 μl of DI water.

Silver telluride nanoparticle stability study.—Silver telluride nanoparticles solutions with a concentration of 0.5 mg mL^{-1} were prepared in water, PBS and PBS + 10% FBS, in triplicate. UV/visible absorption spectra were obtained for each of the solutions in triplicate using the UV/visible spectrophotometer described above. The absorbance spectrum was normalized to a maximum absorbance of 1. The hydrodynamic diameter of the solutions was measured using the Zetasizer described above. The number mean was reported for the hydrodynamic diameter. Solutions were maintained at 25 °C. Both UV/visible spectra and hydrodynamic size were measured at different time points; 0, 1, 3, 7, and 14 days post-dilution.

Inductively coupled plasma optical emission spectroscopy (ICP-OES).—ICP-OES (Spectro Genesis ICP) was used to determine the silver and tellurium concentration in the nanoparticle formulation as previously described.[9,26] In brief, 10 μL of Ag_2Te NP stock solution were placed in 15 mL falcon tubes. The nanoparticles were dissolved in 10% nitric acid. The final silver and tellurium concentrations in the stock solution were obtained by multiplying the concentrations obtained by the ICP-OES by their dilution factor.

Energy dispersive X-ray spectroscopy.—Similar to the transmission electron microscopy methodology, samples were dried onto Formvar carbon-coated copper grids with

200 mesh. The samples were then imaged using a FEI Quanta 600 field emission gun scanning electron microscope equipped with EDX detectors. The equipment was operated at 15 kV.

X-ray powder diffraction.—The diffraction patterns of dried samples were recorded using a Rigaku GiegerFlex D/Max-B X-ray diffractometer. The parameters used while operating the diffractometer were the following: 45 kV, 30 mA, monochromatized Cu Kα radiation wavelength of 1.5406 Å, scan range of 20–60° and 2° per minute scan rate.

Cell assays

Cell culture.—Hep G2 (human hepatocellular liver carcinoma), J774A.1 (murine macrophage), and MDA-MB-231 (human breast cancer) cells were purchased from ATCC (Manassas, VA, USA). Cells were cultured according to the supplier's instructions at 37 °C and 5% CO_2.

***In vitro* cytotoxicity.—**Cell viability studies were performed as described elsewhere.[9,26] In brief, 80 000 cells were seeded in 35 mm dishes with 20 mm bottom well. These cells were incubated for 24 hours in the appropriate cell culture media. After 24 hours, the cell culture media was removed, cells washed with DPBS, and a solution of Ag_2Te, Ag_2S, or Ag nanoparticles diluted in cell media at different concentrations was added. The concentrations used in this experiment were 0.1, 0.5, and 1 mg Ag mL^{-1}. Cells were incubated for 4 hours with the appropriate nanoparticle type and concentrations. Cell viability was determined by LIVE/DEAD assay (Invitrogen Life Technologies, Grand Island, NY). Following the 4-hour incubation period, cells were washed with sterile DPBS, and 400 μL of a solution containing the live cell dye calcein-AM, dead cell dye ethidium-1 homodimer, and nuclei dye Hoechst 33342 in DPBS was added. Cells were incubated with this dye solution for 20 minutes. The cells were then imaged using a Nikon Eclipse Ti-U fluorescence microscope with DAPI (ex: 359, em: 461 nm), FITC (ex: 495, em: 519 nm), and Texas Red (ex: 595, em: 613 nm) filters to image nuclei, live cells, and dead cells, respectively. Four phase images, as well as four images per filter, were taken for each plate. The number of live and dead cells was measured using an in-house developed MATLAB (MathWorks, Natick, MA) code. The viability percentage was determined by the ratio of live cells to dead cells. The relative cell viability (% control) is presented as mean ± standard deviations for each concentration and cell line.

Phantom imaging

Computed tomography.—For CT phantom studies, solutions composed of Ag_2Te NPs, silver ($AgNO_3$), tellurium (Na_2TeO_3), and iodine (iopamidol) at concentrations ranging from 0 to 10 mg of the element of interest per mL were prepared and placed in small vials. PBS was used as a negative control. Each solution was prepared in triplicate. These vials were then secured in a plastic rack. The rack was then submerged in a plastic container holding 21 cm of water to simulate the human abdominal cavity. The samples were imaged using a Siemens SOMATOM Force clinical CT scanner. The images were obtained at tube voltages ranging from 80 to 140 kV in 20 kV increments with a tube current of 360 mA. The field of view used measured 37 × 37 cm while the slice thickness was 0.5 mm and the matrix size was 512 × 512. The obtained images were then analyzed using OsirixMD. The attenuation rates were calculated from the average of three slices per sample.

Dual-energy mammography.—Dual-energy mammography images in a custom-designed wedge phantom (ESI Fig. 20†) were acquired for the study. The phantom consists of a 4 cm-thick continuous gradient section composed of tissue-equivalent materials ranging in composition from 100% glandular tissue to 100% adipose tissue, as previously described.[27] Solutions of Ag_2Te NPs, iodine (in the form of iopamidol), silver salt ($AgNO_3$), and tellurium salt (Na_2TeO_3) were loaded into polyethylene tubes at a concentration of 10 mg of the element of interest per mL; PBS was used as a control. The tubes were inserted into the phantom in the direction of varying tissue composition.

Images of the phantom were then acquired using a prototype DE Hologic Selenia Dimensions mammography system. The imaging system consists of an X-ray source with a tungsten target and an energy-integrating selenium detector. Low-energy (LE) images of the phantom were acquired at 29 kV using a silver filter at 100 mAs; High-energy (HE) images of the phantom were acquired at 38 kV using a copper filter at 90 mAs. Each tube was imaged in triplicate.

DE image subtraction was performed to eliminate variations in the tissue background so that we could differentiate the attenuation of the contrast agent signal from the soft tissue signal. DE images of the phantoms were obtained by a weighted logarithmic subtraction of the HE and LE image pairs. The DE subtraction process and contrast-to-noise (CNR) calculations are described in further detail in our previous works.[26,27]

In vivo experiments

Animal tumor model.—All animal procedures were performed following the Public Health Service (PHS) Policy on Humane Care and Use of Laboratory Animals (Public Law 99–158) in accordance with the University of Pennsylvania Guidelines for Care and Use of Laboratory Animals and approved by the Institutional Animal Care and Use Committee (IACUC) of the University of Pennsylvania under protocol number 805593.

For *in vivo* assessments, an orthotopic tumor model was developed. For this, 2.5×10^6 MDA-MB-231 cells were implanted in the fourth mammary pads of 12 nude female mice. Tumor growth and mouse health were monitored weekly. Tumor volume was measured with calipers and calculated using the following equation: tumor volume = ½ (length × width^2). Mice with tumors with an average volume of 100 mm^3, were injected *via* the tail vein with Ag_2Te NPs or Ag_2S NPs (as a control) at a dose of 250 mg kg^{-1} (190 μL injection volume). This dose was chosen since it is comparable to the iopamidol dose used for patients.[28] Isoflurane was used to anesthetize mice during all experiments.

---

† Electronic supplementary information (ESI) available: Synthesis and characterization of Ag NPs and Ag_2S (TEM micrographs, EDX spectra, UV-visible absorption spectra, XPS spectra, and XRD patterns), FT-IR spectra of the different nanoparticles formulations, 11-mercaptoundecanoic acid coated Ag_2Te as z-potential and stability controls, Ag^+ ion release from Ag_2Te NPs, photograph of DEM phantom, DEM energy pair optimization data, and the quantification of the change in CT attenuation in organs of mice injected with Ag_2S NPs. See DOI: 10.1039/d0nr05489e

Computed tomography.—*In vivo* CT imaging was performed using a Molecubes X-Cube micro-CT scanner. Images were acquired using the following parameters: 50 kVp, 100 µA, 85 ms exposure, and 480 projections. Images were reconstructed through a software provided by the manufacturer and using 100 µm isotropic voxel reconstruction with a noise regularization factor of 3. Mice were scanned before injection, 2 hours post-injection and 24 hours post-injection. The obtained images were analyzed using OsirixMD. For the analysis, ROIs were drawn in the organs of interest and the attenuation values (HU) were recorded. The data is presented as the change in attenuation from pre-injection scans as mean ± standard deviation.

Biodistribution.—The biodistribution experiment was performed in 10 female wild-type mice. 24 hours post-injection, mice were euthanized with CO_2 gas for 10 minutes according to the IACUC approved protocol. Mice were then dissected and tissue from the heart, liver, kidney, spleen, and lungs were collected and their weights were recorded. These tissues were then minced and subjected to acid digestion with 2 mL of nitric acid overnight at 75 °C. The samples were then diluted to a final volume of 10 mL with DI water. The silver and tellurium concentrations were measured for the tissue of mice injected with Ag_2Te NPs while the silver concentration was measured for tissue from mice injected with Ag_2S NPs. The concentration of metals was determined through ICP-OES. An average of 5 mice per group were analyzed. Biodistribution data is presented as mean ± standard error of mean (SEM).

Histology.—Following mice euthanasia, tissues from the major organs (heart, liver, spleen, lung, and kidney) of 2 mice per group, were collected and sliced into 5–6 mm in thickness while placed in chilled PBS. Tissues were immediately fixed in a 10% formalin solution at 4 °C overnight. The samples were then dehydrated, embedded, sectioned, and stained with hematoxylin and eosin (H&E) by the Children's Hospital of Philadelphia Pathology Core.

Statistical analysis

All the experiments were performed independently at least three times. In all figures, data points represent the mean, while the error bars represent standard deviations from the mean or the standard error of mean, as specified. Tukey's multiple comparisons test was used when comparing the stability of Ag_2Te NPs *via* size measurements, the CNR of different solutions in the DEM phantom, and the attenuation rate of the different solutions under CT. Unpaired t-tests were used to compare between cell viability data from Ag and Ag_2Te NPs and when comparing among Ag_2Te and Ag_2S *in vivo* CT attenuation. P values ≤0.05 were considered statistically significant. Statistical analysis was carried out using GraphPad Prism 8 software (San Diego, California USA).

Results and discussion

Synthesis and characterization of Ag_2Te NPs

Ag_2Te nanoparticles were synthesized as depicted in Fig. 1A, where silver nitrate and sodium tellurite were used as silver and tellurium precursors, respectively, and reduced by hydrazine dihydrate. The Ag_2Te NPs were coated with 5K polyethylene glycol thiol (PEG-

SH) for improved stability, biocompatibility, and blood circulation half-life. An electron micrograph from the resulting nanoparticles is shown in Fig. 1B and ESI Fig. 3A.† The nanoparticle core size, measured from the electron micrographs, was found to be 8 ± 2 nm in diameter, while the hydrodynamic diameter was determined to be 17 ± 5 nm *via* DLS measurements. This difference in diameter between the core and the hydrodynamic diameter is expected due to the PEG coating and is in agreement with previous reports of PEG-SH 5K coated nanoparticles. For example, Silvestri, *et al.* has reported a difference of 11 nm while Chen *et al.* reported an increase of 6 nm.[25,29] The *Z*-potential of the nanoparticles was also measured and resulted in −14.9 ± 0.8 mV, which is consistent with other reports of slightly negative or neutral PEGylated nanoparticles.[26,30–32] These results are summarized in Fig. 1D. 11-Mercaptoundecanoic acid (11-MUA) coated Ag_2Te NPs were synthesized as a control nanoparticle with an anionic surface and their *Z*-potential was found to be −48 ± 10 mV (ESI Fig. 1†). To further characterize the Ag_2Te NPs, their UV-vis spectrum was recorded and is shown in Fig. 1C. This broad spectrum reveals a profile characteristic of Ag_2Te nanoparticles where no prominent peak is observed,[16,33] as compared to pure silver nanoparticles (Ag NPs) that have a peak at a wavelength of near 400 nm (ESI Fig. 2†). A high-resolution TEM micrograph of the Ag Te NPs is presented in ESI Fig. 4A.† We further characterized the optical properties of our Ag Te NP formulation, specifically their fluorescence properties. Although other silver chalcogenide nanoparticles have been previously reported to yield fluorescence in the NIR regions, we did not observe fluorescence from this formulation.[34,35] We hypothesize that this is due to the synthesis being carried out in aqueous conditions, which have been previously reported to result in low fluorescent yields.[34,36]

To investigate the composition of the Ag_2Te NPs further, we performed energy dispersive X-ray spectroscopy (EDX). The obtained spectrum is presented in Fig. 2A. In this spectrum, we can observe peaks at an X-ray energy of 2.98 keV, 3.77 keV, and 2.3 keV corresponding to silver, tellurium, and sulfur, respectively. Furthermore, the silver and tellurium peaks show a 2: 1 ratio as expected. ICP-OES measurements also confirmed the 2: 1 ratio of silver to tellurium (data not shown). To further characterize the Ag_2Te NPs, an XRD spectrum was obtained and shown in Fig. 2B. Although broad peaks are observed due to the small size of the nanoparticle core, the strong peaks at 27, 36, and 41 2θ degrees closely matches that of previously reported Ag_2Te XRD patterns,[37,38] while the peak at 24 2θ degrees matches that of PEG.[39,40] Moreover, the Ag_2Te nanoparticles were further characterized using XPS. The resulting spectra are presented in ESI Fig. 5.† This data further confirms the oxidation of Ag and the presence of Te in the samples. The peaks at 366.4 eV and 372.4 eV correspond to Ag 3d 5/2 and Ag 3d 3/2, respectively while those at 570.4 eV and 581.4 eV correspond to Te 3d 5/2 and Te 3d 3/2, respectively.

An important characterization assay to aid in predicting the nanoparticle's *in vivo* performance is the determination of their stability in biologically relevant media. To test this, the nanoparticles were incubated in DI water, PBS, and PBS + 10% FBS to assess their stability in the absence and presence of ions as well as in the presence of both ions and serum proteins. These different solutions were analyzed with UV-vis (Fig. 3A–C) and DLS (Fig. 3D–F) since these two techniques are sensitive to particle size and concentration. The solutions were incubated at room temperature for fourteen days. As shown in Fig. 3, there was no significant change in the UV-vis spectra from the initial incubation time over this time period. Similarly, no significant difference was observed in the hydrodynamic diameter in any of the media tested. These results show the high stability of these nanoparticles in the different conditions and more importantly, in PBS + 10% FBS, which more closely represents the *in vivo* conditions. Complementary, the stability of Ag_2Te NPs was monitored by TEM and XRD. Results are presented in ESI Fig. 6 and 7.† The constant size of the NPs observed in TEM samples and the consistent peaks near 27, 36, and 41 2θ degrees observed with XRD throughout 14 days, further confirms the high stability of the NPs. The peaks at 32, 45, and 56 2θ degrees correspond to NaCl found in PBS, while the peak at 24 2θ degrees corresponds to mPEG-SH 5K, as previously mentioned. ESI Fig. 8† shows the stability of Ag_2Te NPs coated with 11-MUA as a control. The decrease in absorbance for 11-MUA coated Ag_2Te NPS indicates aggregation and therefore inferior stability. To further investigate the degradation of Ag_2Te nanoparticles, we incubated them in water and simulated lysosomal fluid, and measured the release of Ag^+ ions. Results are presented in ESI Fig. 9.† Our results are in agreement with previous reports where Ag_2S released less Ag^+ ions in both conditions compared to Ag nanoparticles.[10] The stability data of PEG-SH 5K coated Ag_2Te NPs, together with other characterizations including the close to neutral *Z*-potential (ESI Fig. 1†), XRD peak at 24 2θ degrees, EDX sulfur peak, and FT-IR (ESI Fig. 10†) suggest the successful PEGylation of the Ag_2Te nanoparticles.[31,39,40]

Ag_2Te nanoparticles show no actute toxicity when incubated with different cell lines

Prior to *in vivo* testing, an *in vitro* assay was conducted where nanoparticles were incubated with different cell types. For this, we studied the effect of the nanoparticles in the viability of specific cell types where they are predicted to accumulate. Due to their size, these nanoparticles are predicted to accumulate in the reticuloendothelial system (RES) organs such as the liver and spleen.[41–43] These nanoparticles should also accumulate in the tumor due to the enhanced permeability and retention (EPR) effect. For this reason, we studied the viability of liver, macrophage, and breast cancer tumor cell lines after incubation with the nanoparticles. Furthermore, the effect of Ag_2Te NPs in these different cell lines was compared to that of pure silver nanoparticles (Ag NPs) which have been shown previously to be toxic to cells due to their release of pure silver ions.[44] As an additional control, the viability of cells after incubation with Ag_2S NPs was also measured. For this, Ag NPs and Ag_2S of the same size and coating were synthesized, and their characterization is presented in ESI Fig. 2–4 and 11–13.† In this experiment, the different cell types were incubated with Ag_2Te NPs and Ag or Ag_2S NPs, as controls, for 4 hours (Fig. 4). The cytotoxic effect of the Ag NPs in all three cell lines at concentrations higher than 0.1 mg Ag mL^{-1} are readily apparent. In contrast, no acute toxicity was observed with Ag_2Te NPs (no significant difference from control) with all three cell lines up to the highest concentration tested (*i.e.* 1 mg Ag mL^{-1}). Similar results were obtained from Ag_2S NPs, in agreement with previous reports.[9] To further look into the biocompatibility of these nanoparticles, we have included the data on the generation of ROS and DNA damage in macrophages and hepatocytes, respectively. Results are presented in ESI Fig. 14 and 15.† Increase ROS generation can be observed for Ag nanoparticles compared to Ag_2Te and Ag_2S at 0.25 mg mL^{-1} whereas at higher concentrations the decrease in ROS is supported by our cell viability data where these cells are no longer viable and thus we detect lower levels of ROS. These data support our cell viability data where no acute toxicity was observed after incubation with Ag_2Te nanoparticles as compared to Ag nanoparticles and the similarity in biocompatibility with Ag_2S nanoparticles.

Ag_2Te NPs generate higher contrast in CT and DEM phantoms compared to silver and iopamidol

The ability of Ag NPs to be used as X-ray contrast agents has been previously investigated.[25,42] It has been shown that Ag NPs can produce slightly less contrast in CT and 40% higher contrast in DEM compared to iodinated molecules currently used in the clinics.[25,45] Similarly, Hsu *et al.* have shown that, using the same imaging equipment as this study and with similar parameters, Ag_2S NPs produce comparable X-ray contrast to Ag.[10] Here, we explored the X-ray contrast of Ag_2Te NPs in two main X-ray imaging modalities: CT and DEM. To test the contrast generation of Ag_2Te NPs in comparison to Ag NPs in both X-ray imaging modalities, experiments using custom-made phantoms were conducted (Fig. 5).

For CT imaging, the phantom containing the different agents was imaged using a clinical CT system at X-ray energies ranging from 80 kV to 140 kV. Fig. 5A shows representative images of the different solutions acquired at an X-ray energy of 80 kV. The attenuation rate for Ag_2Te NPs was higher than that of iopamidol and the other controls, *i.e.* silver nitrate and sodium tellurite, at all studied energies (Fig. 5B).

For the DEM experiments, the LE and HE energy combinations were explored to find the one yielding the highest contrast for Ag_2Te (ESI Fig. 16–20†). From this optimization experiment, we selected the energy combination of 29 kV (LE) and 38 kV (HE). Fig. 5C shows phantom images at LE of 29 kV, HE of 38 kV, and the DE subtraction image. Fig. 5D shows the quantification of the contrast-to-noise ratio (CNR) of the DE subtraction image for the different solutions. Ag_2Te NPs exhibit higher CNR than either silver alone or iopamidol, at this LE and HE energy pair (note that we used silver nitrate as a control, which previous experiments have shown to have identical contrast generation to Ag_2S NPs[10]). Together these phantom studies show that Ag_2Te NPs exhibit higher contrast than either iopamidol or silver nanoparticles without tellurium and suggest that they could be used as X-ray contrast agents. Of course, this observation is due to the presence of tellurium in Ag_2Te NPs, but underscores the benefit resulting from ensuring that both elements in the formulation are contrast generating.

Ag_2Te MPs lead to high CT contrast in breast cancer tumor-bearing mice

Our group has previously developed several silver-based DEM and CT contrast agents.[9,10,26] Among these, silver sulfide nanoparticles (Ag_2S NPs) have shown promise in their use as DEM and CT contrast agents since they produce contrast, *in vivo*, similar to that of pure silver nanoparticles, but without undesired side effects.[9,10] To test the *in vivo* contrast of the Ag_2Te NPs, we developed a mouse model by inoculating MDA-MB-231 breast cancer cells to the mice mammary glands. To compare the *in vivo* contrast generation of Ag_2Te NPs with that of Ag_2S, we developed Ag_2S NPs of the same size and coating (5K mPEG-SH) (ESI Fig. 3 and 10†), since this should yield similar pharmacokinetics and therefore tumor accumulation for both formulations. Tumor-bearing mice were injected with Ag_2Te NPs or

Ag_2S NPs (as a control) at a dose of 250 mg Ag per kg (190 μL injection volume). The tumor-bearing mice were imaged with micro-CT prior to injection and at 2 h post- and 24 h post-injection. Representative CT images of the heart of tumor-bearing mice at different time points injected with Ag_2Te NPs are displayed in Fig. 6A. As presented in Fig. 6B, an increase in contrast is observed in the heart 2 h post-injection. The contrast in the heart can still be observed 24 h post-injection. The long circulation time of Ag_2Te NPs suggests their potential use as blood pool agents for imaging. As expected with nanoparticles of this size, and as shown in ESI Fig. 21,† accumulation was observed in the liver and spleen over 24 hours in both nanoparticle formulations.[26] Moreover, we found the CT attenuation to be higher (compared to pre-injection scans) in the tumors of mice injected with Ag_2Te NPs than in those of mice injected with Ag_2S NPs at 2 h and 24 h post-injection (Fig. 6C and D). No significant difference was found between the NP accumulation in the tumors of mice injected with Ag_2S and Ag_2Te (ESI Fig. 22†). This increase in attenuation is as we expected, given the phantom imaging results.

Ag_2Te NPs accumulate in RES organs and dont' show signs of acute toxicity

To further investigate the nanoparticles biodistribution, mice were sacrificed 24 h post-injection. The organs of both mice groups were collected, and their nanoparticle content was measured through ICP-OES. We found substantial accumulations of Ag_2Te and Ag_2S NPs in the liver and spleen, as expected for nanoparticles of this size[46] (Fig. 7A). We observed similar biodistributions for both nanoparticle formulations, which suggests that the observed differences in contrast could be attributed to the incorporation of tellurium to the formulation. In addition, no significant difference was found between the NP accumulation in the tumors of mice injected with Ag_2S and Ag_2Te (ESI Fig. 23†).

To examine the biocompatibility of Ag_2Te NPs *in vivo* we collected sections of tissue of the tumor-bearing mice at 24 hours post-injection and performed hematoxylin and eosin (H&E) staining. Tissues from mice injected with PBS were used as controls (Fig. 7B). No apparent changes were observed in the tissue structures of Ag_2Te NP-injected mice, with similar morphology found for Ag_2S NPs and PBS-injected mice. These findings support the biocompatibility of the Ag_2Te NPs *in vivo*.

Despite the beneficial optical properties of Ag_2Te NPs, similar to those reported with other silver chalcogenides, these nanoparticles have not been widely explored for their potential biomedical applications. Up-to-date, only one other group has reported the application of these NPs for biomedical applications *in vivo*.[21] In the study, Zhang *et al.* report the intense fluorescence signal and biocompatibility of Ag_2Te quantum dots encapsulated in poly(lactic-*co*-glycolic acid) (PLGA) and coated with cell membrane-derived vesicles. However, this double layer of encapsulation, including the use of a hydrophobic polymer, will limit the possibility for contact of these Ag_2Te quantum dots with mammalian cells compared with the agents reported in our study. Moreover, the concentrations used in their study were quite low compared to the concentrations tested herein. A maximum concentration of particles of 200 μg ml^{-1} in the biocompatibility assays and a silver dose of 2 mg kg^{-1} for *in vivo* experiments were reported. Although these low concentrations are appropriate for more sensitive applications such as fluorescence imaging, many other biomedical applications require much higher doses, such as radiosensitization or photothermal therapy.[47–52] Herein, we have explored Ag_2Te NPs' biomedical application in the setting requiring the highest nanoparticle dose, *i.e.* X-ray imaging.

In this study, we have developed Ag_2Te NPs of hydrodynamic diameter of 17 ± 5 nm. These nanoparticles not only have excellent biocompatibility with the studied cell lines and *in vivo*, but also generate superior X-ray contrast compared to previously reported silver or silver sulfide nanoparticles.[9,10,26,45] This excellent biocompatibility is likely due in part to their PEGylation, which is known to prevent adverse reactions to exogenous materials, and the extremely low solubility product of Ag_2Te. This is evidenced from the *in vitro* biocompatibility studies, where we observed reductions in the viability of cells for pure silver nanoparticles, in agreement with prior reports,[43,51] but not with Ag_2Te or Ag_2S NPs. Histology also shows no acute toxicity in the tissue of mice injected with Ag_2Te. Meanwhile, the high X-ray contrast generating capacity of these NPs, both *in vitro* and *in vivo*, can be largely attributed to the combination of silver and tellurium in the nanoparticles. Our results show higher contrast from Ag_2Te NPs than would be expected from summing the contributions of the individual elements (Fig. 5D). This could be due to a phenomenon reported by Kim *et al.* where nanoparticle contrast agents composed of multiple metals generated higher contrast in CT than the individual elements.[53]

When analyzing the nanoparticle's biodistribution, we observed high accumulation in the liver and spleen 24 hours post-injection. These values are expected due to the nanoparticle's hydrodynamic diameter above the kidney's glomerular filtration threshold (about 5.5 nm).[46] Thus, Ag_2Te NPs are expected to undergo hepatobiliary elimination,[47] which is an extremely slow process and therefore, Ag_2Te NPs are expected to remain in the body for an extended period of time.[54,55] Clinical translation requirements include complete clearance in a reasonable time.[40,53] To improve clinical translatability, reducing the hydrodynamic diameter of Ag_2Te NPs to one allowing kidney/urinary clearance, will be desired. Moreover, while our biocompatibility results are encouraging, more extensive studies, such as blood chemistry, repeated dosing, long-term biodistribution, and assessments in larger animal models will be needed to definitively establish safety. In addition, biocompatibility is known to depend on various factors, such as size, shape, and coating, therefore *in vitro* and *in vivo* studies will need to be completed for any new Ag_2Te NP formulations. Despite the additional work to be done, our studies provide a good indication of the biomedical applications and translatability of these nanoparticles.

Conclusion

For the first time, Ag_2Te NPs have been explored in the *in vivo* setting requiring the highest dose of all biomedical applications: X-ray imaging. Moreover, we have shown the potential utility of these nanoparticles as contrast agents for the screening of breast cancer. Ag_2Te NPs showed no acute toxicity *in vitro* or *in vivo* as shown by cell viability studies and histological analysis, respectively. Their biocompatibility at this very high dose points to the likelihood that Ag_2Te NPs will prove to be biocompatible for their many other possible biomedical applications that require lower doses. Furthermore, CT and DEM phantom studies and *in vivo* CT imaging of breast cancer tumor-bearing mice revealed high contrast generation from Ag_2Te NPs as compared to controls such as a silver salt or Ag_2S NPs. Moreover, higher contrast was observed in tumors of mice injected with Ag_2Te NPs when compared to Ag_2S NPs in CT imaging. Ag_2Te NPs' good biocompatibility, enhanced contrast, as well their blood pool agent characteristics show their potential to be used in biomedical applications and, more specifically, as contrast agents for breast cancer screening.

Supplementary Material

Refer to Web version on PubMed Central for supplementary material.

Acknowledgements

This work was supported by funding from NIH (R01-CA227142-02S1 to LMN and R01-CA227142-02 to DPC), NSF (DGE-1845298 to JCH), and the University of Pennsylvania Department of Radiology. We thank the Electron Microscopy Resource Laboratory (Sudheer Molugu and Biao Zuo) for their technical support with TEM micrographs and Eric Blankemeyer for his help with micro-CT images. Some illustrations were created with BioRender.com.

References

1. Jiao M, Zhang P, Meng J, Li Y, Liu C, Luo X and Gao M, Biomater. Sci, 2018, 6, 726–745. [PubMed: 29308496]
2. Chung S, Revia RA and Zhang M, Adv. Mater, 2019, 1904362.
3. Liu Q, Zhan C and Kohane DS, Bioconjugate Chem, 2017, 28, 98–104.
4. Curry T, Kopelman R, Shilo M and Popovtzer R, Contrast Media Mol. Imaging, 2014, 9, 53–61. [PubMed: 24470294]
5. Bouché M, Hsu JC, Dong YC, Kim J, Taing K and Cormode DP, Bioconjugate Chem, 2020, 31, 303–314.
6. Han X, Xu K, Taratula O and Farsad K, Nanoscale, 2019, 11, 799–819. [PubMed: 30603750]
7. Shapiro EM, Magn. Reson. Med, 2015, 73, 376–389. [PubMed: 24753150]
8. Cole LE, Ross RD, Tilley JM, Vargo-Gogola T and Roeder RK, Nanomedicine, 2015, 10, 321–341. [PubMed: 25600973]
9. Hsu JC, Naha PC, Lau KC, Chhour P, Hastings R, Moon BF, Stein JM, Witschey WRT, McDonald ES, Maidment ADA and Cormode DP, Nanoscale, 2018, 10, 17236–17248. [PubMed: 30191237]
10. Hsu JC, Cruz ED, Lau EKC, Bouché M, Kim J, Maidment AD and Cormode DP, Chem. Mater, 2019, 31, 7845–7854. [PubMed: 33005070]
11. Qin MY, Yang XQ, Wang K, Zhang XS, Song JT, Yao MH, Yan DM, Liu B and Zhao YD, Nanoscale, 2015, 7, 19484–19492. [PubMed: 26531170]
12. Vardar DO, Aydin S, Hocaoglu I, Acar FHY and Basaran N, Chem.-Biol. Interact, 2018, 291, 212–219. [PubMed: 29958870]
13. Tang H, Yang ST, Yang YF, Ke DM, Liu JH, Chen X, Wang H and Liu Y, ACS Appl. Mater. Interfaces, 2016, 8, 17859–17869. [PubMed: 27351208]
14. Gu YP, Cui R, Zhang ZL, Xie ZX and Pang DW, J. Am. Chem. Soc, 2012, 134, 79–82. [PubMed: 22148738]
15. Buketov EA, Ugorets MZ and Pashinkin AS, Russ. J. Inorg. Chem, 1964, 9, 292–294.
16. Yang M, Gui R, Jin H, Wang Z, Zhang F, Xia J, Bi S and Xia Y, Colloids Surf., B, 2015, 126, 115–120.
17. Lu C, Chen G, Yu B and Cong H, Adv. Eng. Mater, 2018, 20, 1700940.
18. Karunamuni R and Maidment AD, Phys. Med. Biol, 2014, 59, 4311–4324. [PubMed: 25029534]
19. Jin H, Gui R, Sun J and Wang Y, Colloids Surf., B, 2016, 143, 118–123.
20. Wang CW, Lin ZH, Roy P and Chang HT, Front. Chem, 2013, 1, 1–5. [PubMed: 24790931]

21. Zhang JJ, Lin Y, Zhou H, He H, Ma JJ, Luo MY, Zhang ZL and Pang DW, Adv. Healthcare Mater, 2019, 8, 1900341.
22. Lusic H and Grinstaff MW, Chem. Rev, 2013, 113, 1641–1666. [PubMed: 23210836]
23. Rose TA and Choi JW, Am. J. Med, 2015, 128, 943–949. [PubMed: 25820169]
24. Shahbazi MA, Faghfouri L, Ferreira MPA, Figueiredo P, Maleki H, Sefat F, Hirvonen J and Santos HA, Chem. Soc. Rev, 2020, 49, 1253–1321. [PubMed: 31998912]
25. Chen H, Paholak H, Ito M, Sansanaphongpricha K, Qian W, Che Y and Sun D, Nanotechnology, 2013, 24, 355101. [PubMed: 23940104]
26. Naha PC, Lau KC, Hsu JC, Hajfathalian M, Mian S, Chhour P, Uppuluri L, McDonald ES, Maidment AD and Cormode DP, Nanoscale, 2016, 8, 13740–13754. [PubMed: 27412458]
27. Lau KC, Hsu JC, Naha PC, Chhour P, Hastings R, Stein JM, McDonald ES, Cormode DP and Maidment AD, Proc. SPIE, 2018, 10718, 107180N.
28. Jochelson MS, Dershaw DD, Sung JS, Heerdt AS, Thornton C, Moskowitz CS, Ferrara J and Morris EA, Radiology, 2013, 266, 743–751. [PubMed: 23220903]
29. Silvestri A, Di Silvio D, Llarena I, Murray RA, Marelli M, Lay L, Polito L and Moya SE, Nanoscale, 2017, 9, 14730–14739. [PubMed: 28948261]
30. Wang W, Wei QQ, Wang J, Wang BC, Zhang SH and Yuan Z, J. Colloid Interface Sci, 2013, 404, 223–229. [PubMed: 23711661]
31. Rahme K, Chen L, Hobbs RG, Morris MA, O'Driscoll C and Holmes JD, RSC Adv, 2013, 3, 6085–6094.
32. Clogston JD and Patri AK, Zeta Potential Measurement, in Characterization of Nanoparticles Intended for Drug Delivery, ed. McNeil SE, Humana Press, Totowa, NJ, 2011, pp. 63–70.
33. Xiao Q, Liang Y, Liu Y, Lu S and Huang S, Luminescence, 2018, 33, 181–189. [PubMed: 28905512]
34. Gui R, Jin H, Wang Z and Tan L, Coord. Chem. Rev, 2015, 296, 91–124.
35. Shen Y, Lifante J, Ximendes E, Santos HD, Ruiz D, Juárez BH, Gutiérrez IZ, Vera VT, Retama JR and Rodríguez EM, Nanoscale, 2019, 11, 19251–19264. [PubMed: 31560003]
36. Shi LJ, Zhu CN, He H, Zhu DL, Zhang ZL, Pang DW and Tian ZQ, RSC Adv, 2016, 6, 38183–38186.
37. Cadavid D, Ibáñez M, Shavel A, Durá OJ, de la Torre ML and Cabot A, J. Mater. Chem. A, 2013, 1, 4864–4870.
38. Gholamrezaei S, Salavati-Niasari M, Ghanbari D and Bagheri S, Sci. Rep, 2016, 6, 20060. [PubMed: 26805744]
39. Mukhopadhyay A, Joshi N, Chattopadhyay K and De G, ACS Appl. Mater. Interfaces, 2012, 4, 142–149. [PubMed: 22111689]
40. Ahmad MB, Tay MY, Shameli K, Hussein MZ and Lim JJ, Int. J. Mol. Sci, 2011, 12, 4872–4884. [PubMed: 21954331]
41. Hoshyar N, Gray S, Han H and Bao G, Nanomedicine, 2016, 11, 673–692. [PubMed: 27003448]
42. Yu M and Zheng J, ACS Nano, 2015, 9, 6655–6674. [PubMed: 26149184]
43. Feng Q, Liu Y, Huang J, Chen K and Xiao K, Sci. Rep, 2018, 8, 2082. [PubMed: 29391477]
44. Durán N, Silveira CP, Durán M and Martinez DS, J. Nanobiotechnol, 2015, 13, 55.
45. Karunamuni R, Tsourkas A and Maidment AD, Br. J. Radiol, 2014, 87, 20140081. [PubMed: 24998157]
46. Dong YC, Hajfathalian M, Maidment PSN, Hsu JC, Naha PC, Si-Mohamed S, Breuilly M, Kim J, Chhour P, Douek P, Litt HI and Cormode DP, Sci. Rep, 2019, 9, 14912. [PubMed: 31624285]
47. Li C, Yang XQ, Zhang MZ, Song YY, Cheng K, An J, Zhang XS, Xuan Y, Liu B and Zhao YD, Theranostics, 2018, 8, 5662–5675. [PubMed: 30555572]
48. Xu Y, Wang X, Cheng L, Liu Z and Zhang Q, Chem. Eng. J, 2019, 378, 122025.
49. Yang K, Hu L, Ma X, Ye S, Cheng L, Shi X, Li C, Li Y and Liu Z, Adv. Mater, 2012, 24, 1868–1872. [PubMed: 22378564]
50. Paunesku T, Gutiontov S, Brown K and Woloschak GE, Cancer Treat. Res, 2015, 166, 151–171. [PubMed: 25895868]

51. Laprise-Pelletier M, Simão T and Fortin MA, Adv. Healthcare Mater, 2018, 7, 1701460.

52. Zhu B, Li Y, Lin Z, Zhao M, Xu T, Wang C and Deng N, Nanoscale Res. Lett, 2016, 11, 198. [PubMed: 27075340]

53. Kim J, Silva AB, Hsu JC, Maidment PS, Shapira N, Noël PB and Cormode DP, Chem. Mater, 2020, 32, 381–391. [PubMed: 33005071]

54. Zhang YN, Poon W, Tavares AJ, McGilvray ID and Chan WCW, J. Controlled Release, 2016, 240, 332–348.

55. Choi HS, Liu W, Misra P, Tanaka E, Zimmer JP, Ipe BI, Bawendi MG and Frangioni JV, Nat. Biotechnol, 2007, 25, 1165–1170. [PubMed: 17891134]

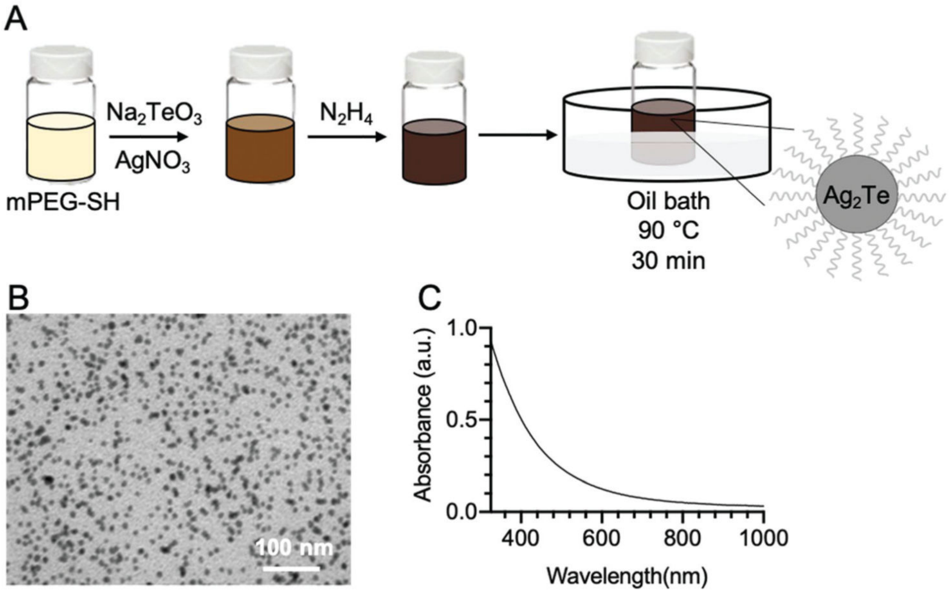

D

Core diameter	Hydrodynamic diameter	Z-potential
8 ± 2 nm	17 ± 5 nm	-14.9 ± 0.8 mV

Fig. 1.

Ag_2Te nanoparticle synthesis and characterization. (A) Schematic depiction of Ag_2Te NP synthesis. (B) Transmission electron micrograph of Ag_2Te NPs. (C) UV-visible absorbance spectrum of Ag_2Te NPs. (D) Table summarizing Ag_2Te NP core diameter, hydrodynamic diameter, and *z*-potential values.

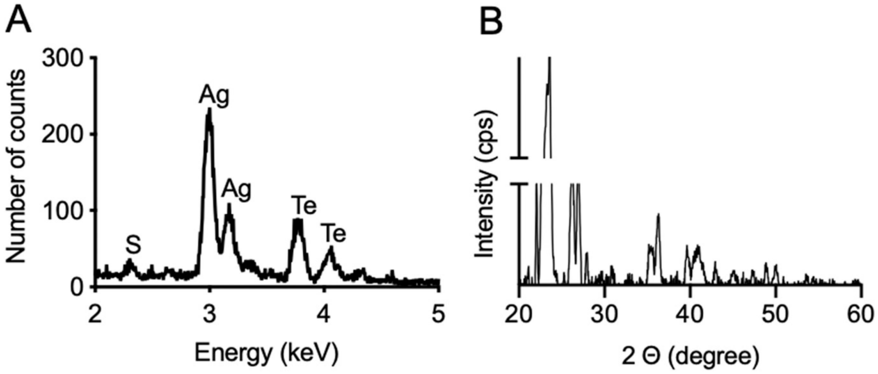

Fig. 2.

(A) Energy dispersive X-ray spectrum of Ag_2Te nanoparticles. (B) XRD spectrum of Ag_2Te nanoparticles.

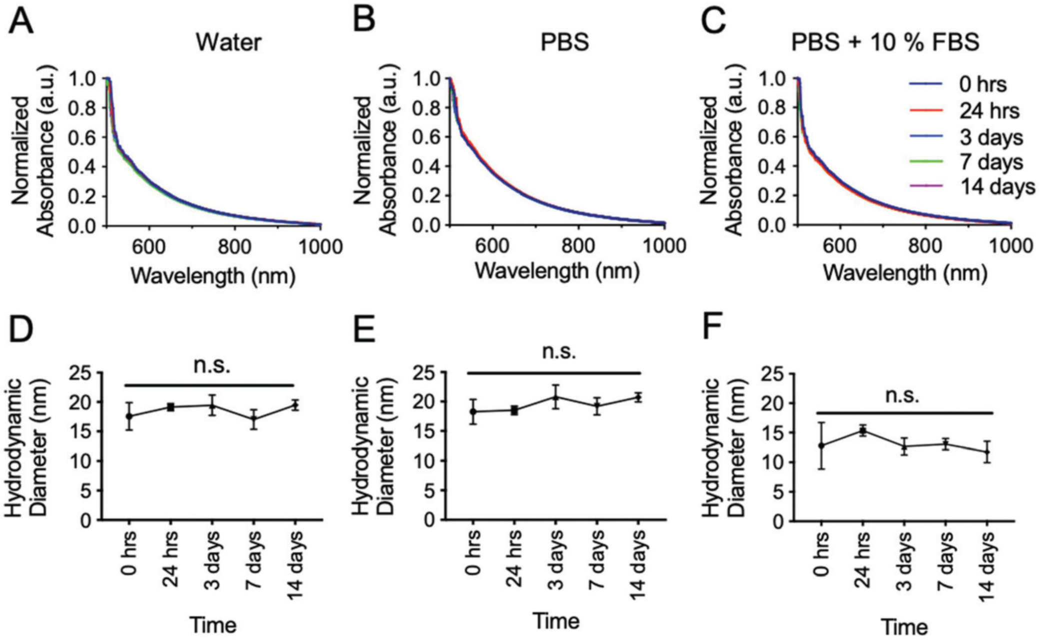

Fig. 3.

UV-Vis spectra of Ag_2Te nanoparticles incubated in (A) DI water, (B) PBS and (C) PBS + 10% FBS for 14 days. The dark blue curve shows data from day 0, red from 24 h, blue from 3 days, green from 7 days, and purple from 14 days post-incubation in the different media. The hydrodynamic diameter of Ag_2Te nanoparticles in (D) DI water, (E) PBS, and (F) PBS + 10% FBS. Data is presented as the mean, while the error bars represent standard deviations.

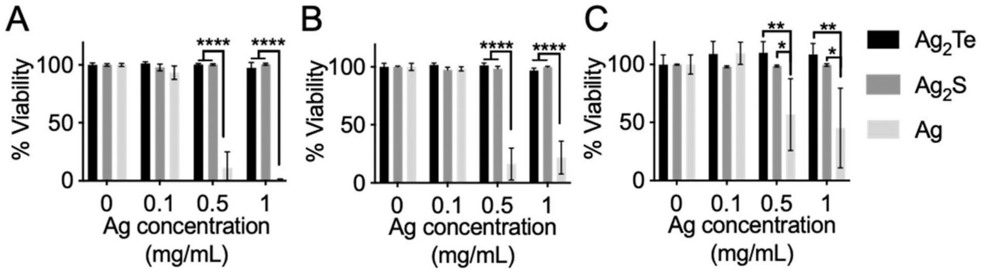

Fig. 4.

Viability of (A) Hep G2, (B) MDA-MB-231 and (C) J774A.1 cells after incubation with Ag_2Te (black bars), Ag_2S (dark gray) or Ag NPs (silver bars) for 4 hours. Error bars represent standard deviations. **P*-value <0.05. ***P*-value ≤0.01 *****P*-value <0.0001.

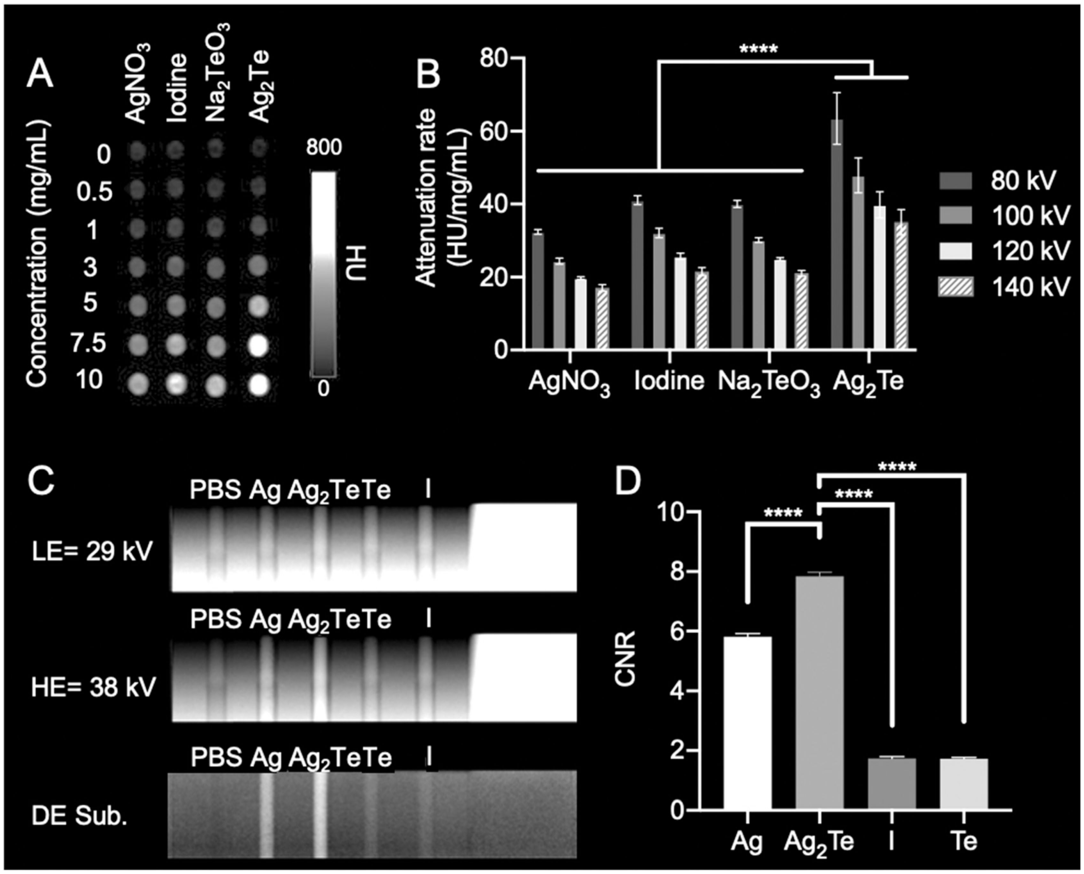

Fig. 5.

In vitro imaging with CT and DEM. (A) CT phantom image at an energy of 80 kV. (B) Quantification of the CT attenuation rate of the different solutions at different energies. Error bars represent standard deviation. (C) DEM phantom imaging at a LE of 29 kV, HE of 38 kV, and DEM subtraction image. (D) DEM phantom image contrast-to-noise ratio (CNR) quantification. $****P \leq 0.0001$. Ag denotes $AgNO_3$ salt, Te denotes Na_2TeO_3 salt, and I denotes iopamidol. PBS was used as a negative control. The different solutions had a concentration of 10 mg of the element of interest per mL (Ag_2Te NPs had a concentration of 10 mg of Ag mL^{-1} to facilitate comparison).

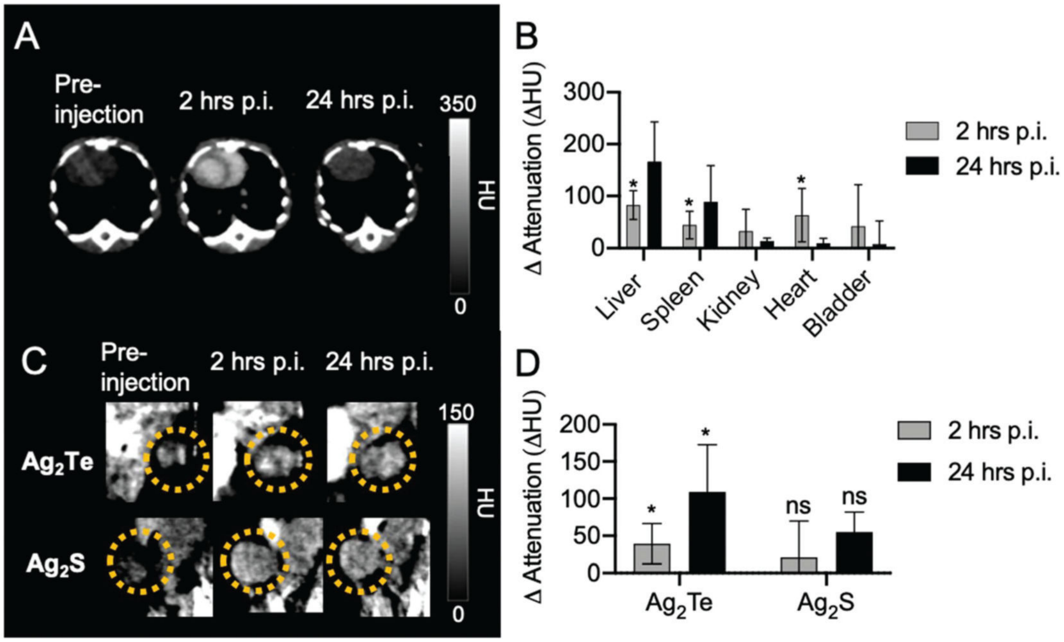

Fig. 6.

In vivo CT imaging of breast cancer tumor-bearing mice. (A) Representative CT scan images at the level of the heart from a mouse injected with Ag_2Te NPs, at different time points: pre-injection, 2 h post-injection (2 h p.i.) and 24 h post-injection (24 h p.i.). (B) Quantification of the change in CT attenuation (difference between pre-injection and the different time point images) in the major organs of mice injected with Ag_2Te NPs. (C) Representative images of CT scans from tumor-bearing mice injected with Ag_2Te NPs (top row) or Ag_2S NPs (bottom row). Tumors are highlighted in yellow circles. ROIs matching the outlines of the tumors were used for image analysis. (D) Quantification of the change in CT attenuation in the tumors from mice injected with Ag_2Te or Ag_2S NPs. Error bars represent standard deviation. Statistical comparisons are versus pre-injection scans. $*P <$ 0.05.

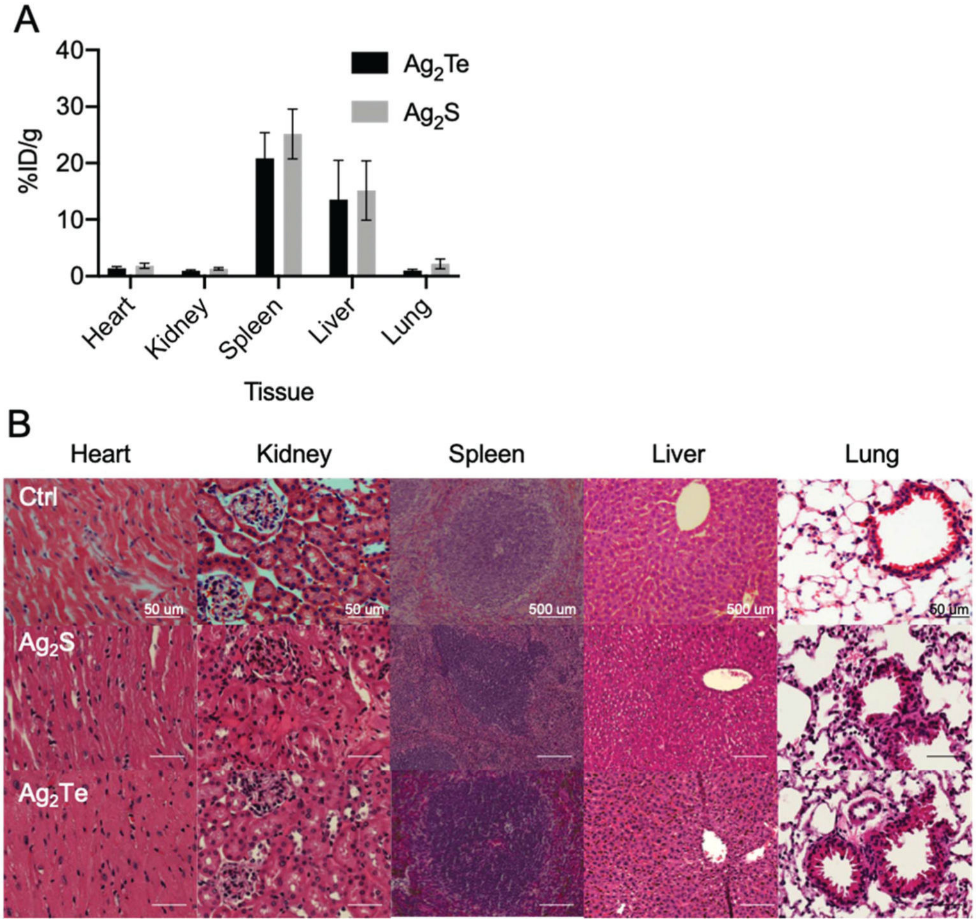

Fig. 7.

(A) Biodistribution of Ag_2Te and Ag_2S NPs in major tissues and organs of injected mice. Data is presented as percent injected dose per gram (%ID/g). Error bars represent standard error of mean (SEM). (B) Representative micrographs of tissue from major organs, after H&E staining, of mice injected with saline (top row), Ag_2S NPs (middle row), and Ag_2Te NPs (bottom row).